

<https://doi.org/10.1038/s43247-024-01305-x>

Turbulent particle-gas feedback exacerbates the hazard impacts of pyroclastic density currents

Check for updates

Daniel H. Uhle¹ , Gert Lube¹, Eric C. P. Breard^{2,3}, Eckart Meiburg⁴, Josef Dufek³, James Ardo¹, Jim R. Jones⁵, Ermanno Brosch¹, Lucas R. P. Corna¹ & Susanna F. Jenkins⁶

Causing one-third of all volcanic fatalities, pyroclastic density currents create destruction far beyond our current scientific explanation. Opportunities to interrogate the mechanisms behind this hazard have long been desired, but pyroclastic density currents persistently defy internal observation. Here we show, through direct measurements of destruction-causing dynamic pressure in large-scale experiments, that pressure maxima exceed theoretical values used in hazard assessments by more than one order of magnitude. These distinct pressure excursions occur through the clustering of high-momentum particles at the peripheries of coherent turbulence structures. Particle loading modifies these eddies and generates repeated high-pressure loading impacts at the frequency of the turbulence structures. Collisions of particle clusters against stationary objects generate even higher dynamic pressures that account for up to 75% of the local flow energy. To prevent severe underestimation of damage intensities, these multiphase feedback processes must be considered in hazard models that aim to mitigate volcanic risk globally.

Dilute pyroclastic density currents (PDCs) are lethal and recurrent hazards from volcanoes^{1–5}. Over 200 million people are directly endangered by these multiphase flows of hot volcanic particles and gas^{6–8}. Over the past decade alone, and despite strong advances in understanding volcanic hazards, PDCs caused more than a thousand fatalities and significant damage to infrastructure globally^{9–13}. So, how can we learn to forecast PDC hazards more accurately? The key hazard agents of PDCs are the volcanic particles carried inside them. As the main driver of PDC motion, particle concentration controls flow speed, destructive power and reach^{14–22}. Carrying most of the thermal energy, particles are also important for PDC burn hazards, while the readily respirable particles cause inhalation injury and asphyxia^{23,24}. To model and mitigate against PDC hazards we must learn to better understand the behaviour of particles, more specifically their motion and sedimentation, inside flows^{1,3–5}.

However, there is a fundamental roadblock hindering this endeavour: the motion of particles within a PDC is modified through complex, long-hypothesized but poorly understood coupling and feedback mechanisms between particle and gas phases^{4,25–28}. Unlike a homogenous suspension of particles in a fluid, these interactions modify the flow and turbulence

structure in PDCs, leading to particle clustering, enhanced sedimentation, high pore-pressure and fluidization^{29–35}. Recent advances through large-scale PDC experiments discovered that these interactions focus particles, and thus mechanical and thermal energies, into large eddies, mesoscale turbulence structures and internal gravity waves³⁶. However, how the feedback mechanisms between particles and gas control the runout and hazard behaviour of PDCs remains unknown. The opportunity to explore the multiphase physics of PDCs is long desired, but their ferocity, opacity and unpredictability hampers direct observation and measurements of their internal characteristics.

An important example of the large uncertainties for hazard planning that result from this gap in understanding is forecasting of the destruction-causing dynamic pressure of PDCs. To estimate local values of dynamic pressure, researchers have systematically mapped the degree of damage to infrastructure and vegetation in the aftermath of volcanic eruptions^{37–40}. Another approach uses relationships between sediment transport and resulting deposit characteristics in turbulent fluid flow to estimate local time-averaged values of flow velocity and density, which together define dynamic pressure^{26,41–43}. Recently, direct measurements in large-scale

¹Volcanic Risk Solutions, Massey University, Palmerston North, New Zealand. ²School of Geosciences, The University of Edinburgh, Edinburgh, UK. ³Department of Earth Science, University of Oregon, Eugene, OR, USA. ⁴Department of Mechanical Engineering, University of California at Santa Barbara, Santa Barbara, CA, USA. ⁵School of Food and Advanced Technology, Massey University, Palmerston North, New Zealand. ⁶Earth Observatory of Singapore, Asian School of Environment, Nanyang Technological University, Singapore, Singapore. e-mail: d.uhle@massey.ac.nz

experiments, natural PDCs and snow avalanches demonstrated that dynamic pressure calculated from turbulent fluctuations in velocity and density exceed field- and theory-derived pressure estimates³⁶. This finding demonstrates the importance of turbulent multiphase flow in volcanic hazard assessments and raises caution regarding the applicability of current approaches, which use (time) average flow properties.

Here we present the first high-resolution direct measurements of destruction-causing dynamic pressure in large-scale PDC experiments to interrogate how dynamic pressures form and evolve in PDCs. These measurements reveal that dynamic pressure reaches pronounced maxima in the peripheries of turbulence structures and generate regular pulses of high dynamic pressure at the characteristic frequency of these structures. This occurs through turbulent gas-particle feedbacks as particles, whose ratio of characteristic response time to fluid motion to the characteristic timescale of fluid motion is less than or equal to one, cluster at the margins of eddies. We demonstrate that this process results in two different types of dynamic pressure effects with distinct hazard impacts to life and infrastructure. Importantly, the resulting energy spectra of dynamic pressure are characterized by peak pressure values that largely exceed pressure estimates based on bulk flow characteristics, which are currently used for hazard assessments.

Results

Synthesizing pyroclastic density currents and measuring dynamic pressure in large-scale experiments

Over the last decade, the development of large-scale experimental facilities to synthesize scaled analogues of PDCs^{16,44–46} has enabled a novel approach to study their internal flow characteristics under safe conditions. The experimental apparatuses in Italy⁴⁵ and New Zealand⁴⁴, which use heated natural volcanic material, lend themselves to the interrogation of the scaled fluid mechanic and thermodynamic processes inside fully turbulent PDC analogues. Here we report the results of direct measurements of dynamic pressure inside large-scale experimental PDCs conducted at the New

Zealand facility PELE (the Pyroclastic flow Eruption Large-scale Experiment). At PELE, experimental PDCs are generated by the controlled gravitational collapse of a suspension of hot volcanic particles and air from an elevated hopper into an instrumented runout section (Supplementary Fig. 1; Supplementary Movie). For the experiments reported here, we used a 0.7 m³ hopper in which a 124 kg mixture of natural volcanic particles was heated to 120 °C (the ambient temperature was 15 °C) over a period of 72 h to allow for thermal equilibration and evaporation of residual moisture inside the pre-dried mixture.

The volcanic material comprises a mixture of two well-characterised deposits of PDCs of the 232 CE Taupo eruption in New Zealand⁴⁷. The main components of the mixture are highly vesicular pumice, glass shards, free crystals and rare lithic particles. The mixture has a weakly bimodal grainsize distribution ranging from 2 µm to 16 mm, with a main mode at 250 µm and a minor mode at 11 µm. The particle density distribution ranges from c. 300–2,600 kg m⁻³ and is skewed towards low densities. Further details of the material characteristics are provided in Supplementary Fig. 1 and in the Methods section.

The hopper is lifted to a vertical drop height of 7 m. It is mounted onto four load cells recording its mass discharge, which in this case lasts c. 4.6 s at an average discharge rate of c. 27 kg s⁻¹. On impact into a 0.5 m-wide and 12 m-long flume with a slope of 6°, the aerated particle-air mixture forms a channelized dilute gravity current with an initial front velocity of c. 5.5 m s⁻¹ and, on average, particle volume concentration of c. 0.25 vol.%. The flow is characterized by a leading, c. 1.1–2 m thick gravity current head, which is trailed by a gravity current wake that overlies a c. 0.9–1.6 m thick gravity current body, and followed by a c. 1.8–3.5 m thick gravity current tail region (Fig. 1a, b). Downstream of the inclined flume section, the experimental PDC propagates to 17 m along a horizontal, 0.5 m wide channel-confined section before spreading across an unconfined horizontal concrete pad. Around 8 s after impact, the vertically density-stratified current has propagated 23.5 m, slowed to c. 0.5 m s⁻¹ and has emplaced approximately 99.7% of its total deposit volume. At 24 m, the depth- and time-integrated

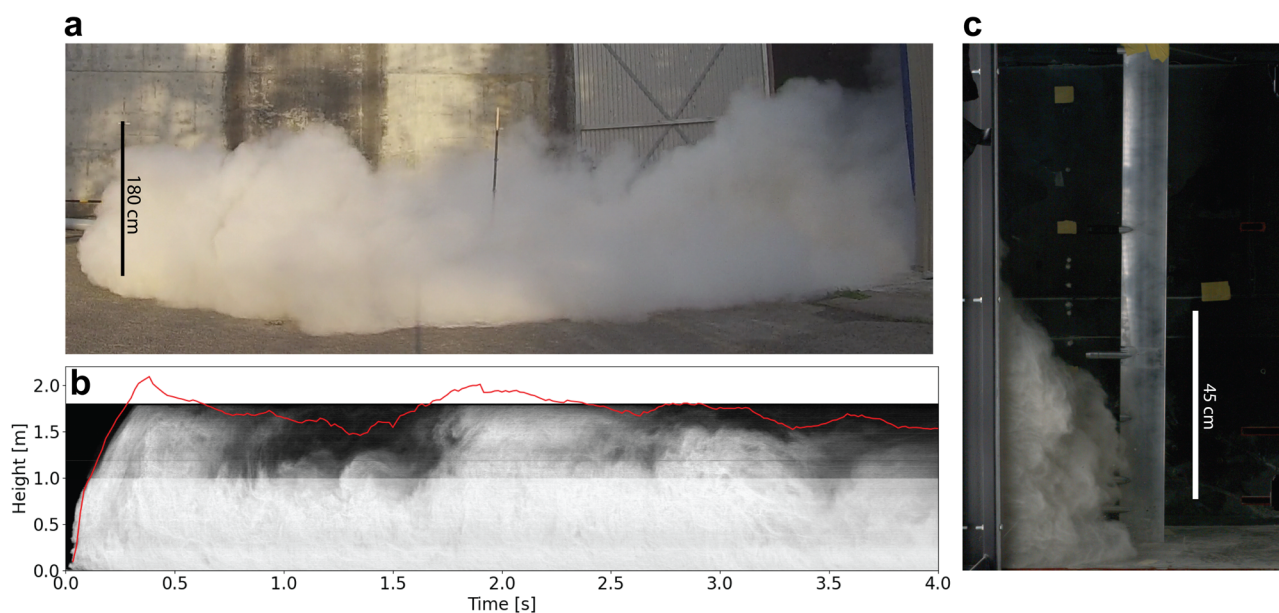


Fig. 1 | Synthesizing pyroclastic density currents and dynamic pressure measurements in large-scale experiments. **a** The time-variant flow structure of the experimental PDC during channel confined propagation along a proximal measurement profile, which is located at 1.8 m downstream from impact of the hot mixture of volcanic material and air with the channel. The height-time kymograph is obtained by the stacking of vertical columns of pixels recorded by a high-speed camera at the static observer location. Pixel brightness correlates positively with, both, bulk flow particle volume concentration and the abundance of highly reflective coarse-grained pumiceous glass shards and plagioclase crystals. At this location, the density current structure is

fully developed comprising a leading head with a wake in its rear and a trailing density current body. The density current tail region is not shown. **b** Lateral view of the frontal c. 7 m of the advancing experimental PDC across the unconfined distal runout section approximately 1.5 m before buoyancy reversal. The red line shows the time-variant height of the upper flow boundary. **c** Snapshot of the front of the experimental PDC approaching one of the wing-shaped vertical profiles of dynamic pressure sensors. The shape of the wings is designed to reduce flow detachment and formation of a turbulent wake behind the profile. The sensing elements of the piezoelectric dynamic pressure sensors protrude, upstream from the wing, into the approaching density current.

particle volume concentration has decreased to values smaller than 0.01 vol.% due to both deposition and entrainment of ambient air; the current becomes positively buoyant and finally ascends as a series of thermals along the flow length (Supplementary Movie).

To investigate the origin and evolution of dynamic pressure inside the experimental PDCs, seven vertical, airfoil-shaped profiles with up to six piezo-electric dynamic pressure sensors, which comprise circular, 15 mm diameter frontal steel diaphragms, were placed into the flow centerline at runout distances of 1.8, 3.35, 5.4, 9.6, 12, 16 and 20 m (Fig. 1c). Measurements of time (*t*)-variant dynamic pressure $P_{dyn}(t, z)$ are recorded at a frequency of 1 kHz, and are complemented by measurements of time series, in vertical profiles, of flow velocity $u(t, z)$, particle volume concentration $C_s(t, z)$, flow density $\rho_C(t, z)$, flow temperature and grain-size distribution, where z is the height above the flow base in the direction perpendicular to slope (see methods for details). Flow velocity components $u(t, z)$ are measured using high-speed video at 0.5 kHz through the flume's tempered glass sides. The sidewalls introduce boundary effects that are not present in unconfined real-world flows and in the flow centerline of the experimental flows where dynamic pressure is measured. We minimize these boundary effects through the use of hydraulically smooth sidewalls (i.e., thickness of laminar layer/wall roughness >1) while the flow's Reynolds number, which is inversely related to the thickness of the viscous boundary layer, is high ($Re = 1.5 \times 10^6$). Velocity data together with measurements of time-variant and height-variant grain-size distribution, flow density and temperatures allow for an independent measurement of dynamic pressure, defined as:

$$P_{dyn_Bernoulli} = \frac{1}{2} \rho_C |u|^2, \quad (1)$$

where $|u|$ is the magnitude of the local time-variant velocity.

The experimental PDCs generated under these conditions scale well to natural dilute fully turbulent PDCs (i.e., pyroclastic surges or blasts; see a comparison of scaling parameters for natural and experimental PDCs in Supplementary Table 1). Amongst the non-dimensional products of characteristic length-, time and temperature-scales we highlight the Reynolds number (comparing inertial and viscous forces) reaching values of 1.5×10^6 , Stokes number (comparing particle time-scale to turbulent flow time-scale) of $10^{-3} - 10^0$, Stability number (comparing time-scales of particle settling and turbulent fluid motion) of $10^{-2} - 10^1$, Richardson number (characterizing the stability of stratification in turbulent flows) of $10^{-2} - 10^1$, and thermal Richardson number (assessing the ratio of forced and buoyant convection) of 0.02–4.5. The overlap of ranges in Reynolds, Stokes and Stability numbers in experimental and natural PDCs ensures that the complete range of particle-gas feedback mechanisms and turbulent particle transport is reproduced.

Two types of dynamic pressure

Figure 2a and b depict a typical example of the time series of dynamic pressure inside the experimental PDCs (here for the vertical profile 2 at a runout distance of 3.35 m at approximately mid-flow height of 0.45 m from the flow base). The local time-averaged dynamic pressure takes a value of 45 Pa, while maximum values reach several kilopascals. The wide discrepancy between average and maximum pressures, as well as the absolute values of recorded maximum pressure are surprising. Recent analysis of dynamic pressure in experimental PDCs using measurements of flow velocity and flow density and Eq. 1 showed that turbulent fluctuations in velocity and density generate dynamic pressures that exceed average values by a factor of 3–5³⁶. This coincides with our measurements of dynamic pressure through velocity and density time-series (that is $P_{dyn_Bernoulli}$) and Eq. 1 giving maximum and average values of 79 and

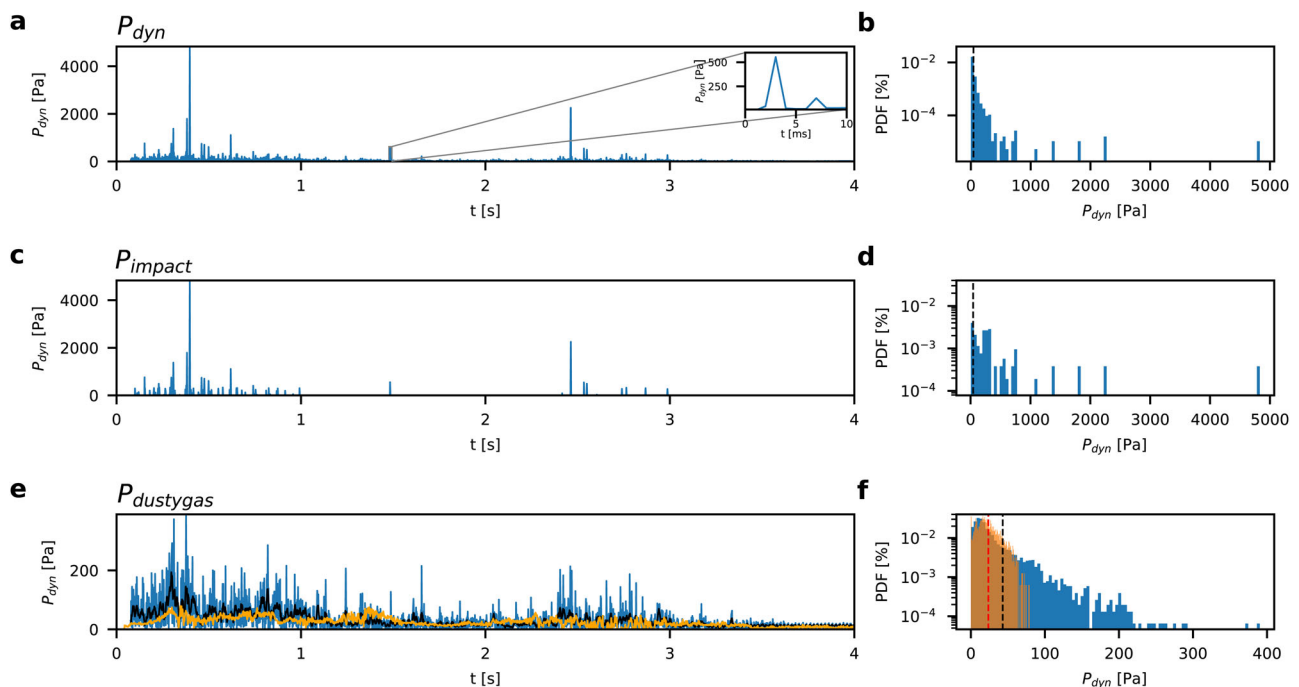


Fig. 2 | Two types of dynamic pressure and their probability density spectra. All measurements of dynamic pressure shown in this figure are obtained at the location of 3.35 m from impact at a height 0.45 m above the flow base. **a** Variation of the entire dynamic pressure P_{dyn} as a function of time as recorded by piezoelectric sensor and the corresponding probability density function shown in **b**. The pressure signal of P_{dyn} shows abundant near-instantaneous high-pressure peaks of several hundreds to thousands of Pascal, which are characterized by pressure increases in less than one millisecond. The inset highlights an example of one of the near-instantaneous high-pressure signals, which are associated with impacts from individual particles with the pressure sensor. **c** Variation of the partial dynamic pressure signal P_{impact} as a

function of time recorded by the piezoelectric sensor, which shows only those parts of the entire pressure signal P_{dyn} that are associated with near-instantaneous pressure peaks. **d** The probability density function of P_{impact} . **e** Variation of the partial dynamic pressure signal $P_{dustygaz}$ as a function of time, which is the dynamic pressure of the continuous dusty gas phase computed as the difference between $P_{dyn}(t)$ and $P_{impact}(t)$ via Eq. (2). The black line shows a 20-millisecond average of the timeseries $P_{dustygaz}$ (depicted in blue) The orange line shows the corresponding timeseries of the dynamic pressure $P_{Bernoulli}$, computed independently from timeseries of flow velocity and flow density via Eq. (1). **f** probability density functions of $P_{dustygaz}$ (blue) and $P_{Bernoulli}$ (orange).

24 Pa (i.e., a ratio of c. 3.3), respectively. In stark contrast, time-averaged (45 Pa) and maximum dynamic pressures (4830 Pa) recorded by the dynamic pressure sensors (Fig. 2a) differ by two orders of magnitude. They can, therefore, not be explained by turbulent fluctuations in velocity and density of the multiphase flow. Thus, from the perspective of understanding and mitigating hazard impacts of PDCs, an important question arises regarding the origin and nature of these unexpectedly large pressures.

An important clue is given by the form of those pressure signals that exceed the theoretical values of dynamic pressure calculated through turbulent fluctuations of flow velocity and density through Eq. 1. These high-pressure signals are characterized by an abrupt pressure increase to a maximum in less than one millisecond (inset of Fig. 2a; the sensor response time (12 μs) ≪ sampling rate (1 ms)). Furthermore, we determined that in all occurrences of these near-instantaneous high-pressure signals, the rate of pressure change with time was always larger than c. 220 Pa ms⁻¹. These characteristics in the form of pressure signals are consistent with impacts of individual particles on the pressure sensor. Considering particle diameters and size-averaged particle densities determined from flow samples, and local velocities measured in high-speed video, theoretical values of dynamic pressure caused by impacts of individual particles can be estimated (Supplementary note 1 and Supplementary Fig. 3). At time-averaged local velocities, impacts of particles with diameters larger than c. 100 μm generate dynamic pressures larger than 500 Pa, and thus, considerably larger than theoretical values of dynamic pressure calculated through turbulent fluctuations of flow velocity and density and Eq. 1. Maximum measured values of dynamic pressure (e.g., 4.8 kPa at profile 2) can be explained by impacts of, either, low-density pumiceous particles with particle diameters larger than c. 2 millimeters or abundant high-density plagioclase particles with particle diameters larger than c. 600 μm. Hence, the near-instantaneous high-pressure signals are explained by individual particle impacts.

This finding allows a sub-division of the total dynamic pressure signal P_{dyn} into the dynamic pressure associated with impacts from individual particles P_{impact} (Fig. 2c and d) and the dynamic pressure of the (continuous) dusty gas phase $P_{dusty\ gas}$ (Fig. 2e) where:

$$P_{dyn} = P_{dusty\ gas} + P_{impact} \quad (2)$$

Probability density functions of $P_{dusty\ gas}$ and $P_{dyn_Bernoulli}$ coincide markedly well (Fig. 2f). This justifies the subdivision of the total dynamic pressure into its continuous dusty gas, $P_{dusty\ gas}$ and particle impact, P_{impact} components. Furthermore, the piezoelectric signal of the dynamic pressure sensor has a superior temporal resolution (1 kHz) in comparison to the timeseries of dynamic pressure $P_{dyn_Bernoulli}$ computed, via Eq. 1, from timeseries of flow density data (with a sampling rate of 20 Hz) and velocity (sampled at 0.5 kHz). Thus, the piezoelectric signal shows a much more detailed record of the dynamic pressure of the continuous dusty gas phase in the high-pressure end of its spectrum.

Despite the strong differences in pressure ranges between the dynamic pressures of the dusty gas phase (up to 390 Pa at profile 2) and particle impacts (up to 4.8 kPa at profile 2), the probability density functions and the time-series of both signals, and hence that of the total dynamic pressure, share two characteristics: first, the pressure distributions are strongly skewed towards large pressures (Fig. 2b, d and f). Second, largest pressures and highest occurrences of large pressures occur during passages of the head (c. 0–1 s in Fig. 2a, c and e) and mid-body regions (c. 2.4–3 s in Fig. 2a, c and e) of the experimental PDC. For the dynamic pressure of particle impacts P_{impact} time-series of the rate of particle impacts, R , provide further insights (Fig. 3 e–h). Along flow runout, the rate of particle impacts, at approximately mid-flow height (i.e., at $z = 0.45$ m), decays strongly from more than 275 Hz at a distance of 1.8 m, to 95 Hz at 5.4 m and no recorded impacts at 9.6 m and beyond. This suggests that dynamic pressure signals associated with impacts from individual particles are limited to particles with a critical

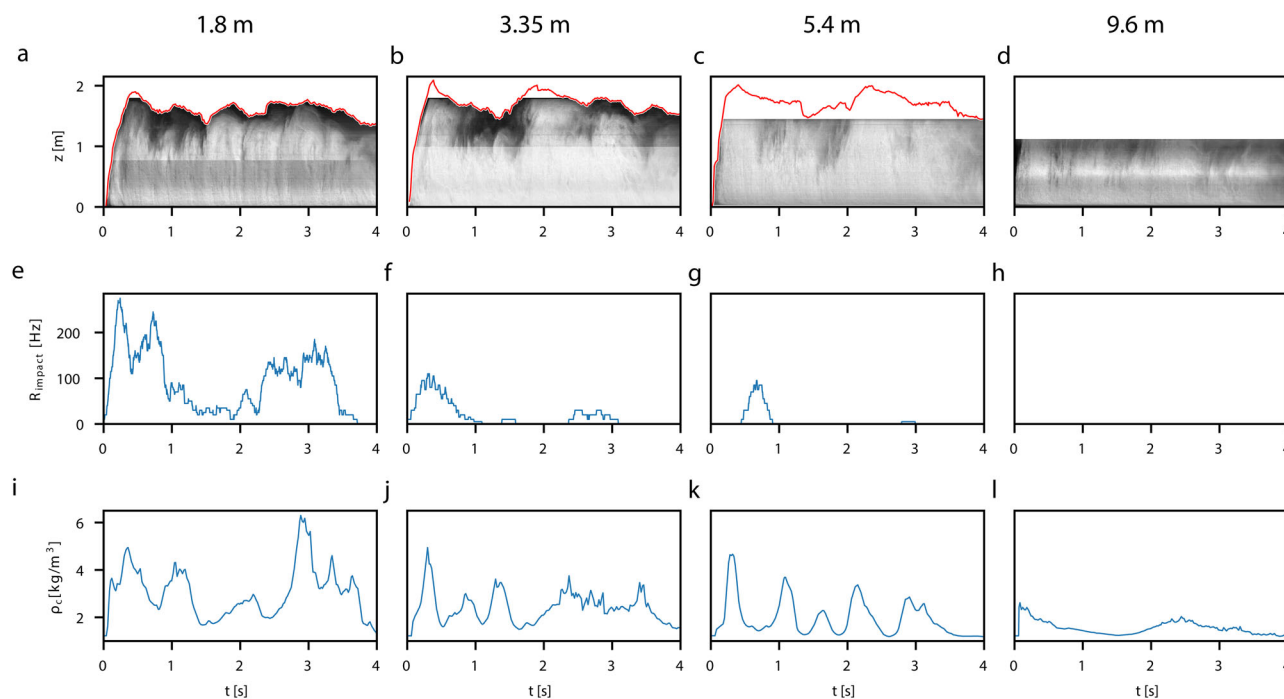


Fig. 3 | Spatiotemporal variation of the frequency of particle impacts. The time-variant flow structure of the experimental PDC at four different distances from impact with the channel at 1.8 m (a), 3.35 m (b), 5.4 m (c) and 9.6 m (d). As in Fig. 1a, the height-time kymograph plots are generated by the stacking of vertical columns of pixels recorded by high-speed cameras at the static observer locations. **e–h** Time-series of the frequency of particle impacts f_{impact} at the four different distances. The frequency of particle impacts is computed through convolution of time series of

binary impacts using a box function with a duration of 200 ms. Time series of binary impacts, shown in Fig. 5, were generated by assigning times of occurrences of particle impacts a value of 1 and times without impacts a value of zero. Due to the sampling rate of 1 kHz, impact rates of up to 500 Hz can be resolved. The frequency strongly declines with distance. **i–l** Timeseries of the depth-integrated flow density $\rho_C(t)$ at the four different distances. The regular low-frequency oscillations in flow density are positively correlated in time with the oscillations of particle impacts.

minimum momentum. We note that the pattern of decay of the number of particle impacts with runout distance is similar to the decay of particles with diameters of 125–500 μm in flow samples (Fig. 4). This is the grain-size range that constitutes the coarse tail of flow grain-size distributions in proximal to distal runout reaches.

The low numbers of particle impacts at medial to distal profile locations (i.e., > 10 m) limit further analysis. However, at the proximal profiles, impact numbers are sufficiently large to see that the rate of impacts obeys a regular low-frequency oscillation (Fig. 3e and f), which is positively correlated in time with a low-frequency oscillation in flow density (Fig. 3i and j; i.e. the number of impacts is large when flow density is high).

Figure 5 depicts timeseries of particle impacts in binary form (i.e., times during which an impact occurs are assigned a value of 1, and times where no impacts occur a value of zero). This shows that if a particle impact occurs, it is typically followed by multiple further impacts. By contrast, isolated single particle impacts are rare. The mean of the number of successive, in other words, clustered impacts ranges from 2–14 impacts with an average number of clustered impacts of c. 4.

Energy spectra of dynamic pressure from particle impacts and dusty gas

Recently, low-frequency oscillations in flow density, velocity and hence dynamic pressure have been linked to the occurrence of large-scale coherent turbulence structures inside experimental and real-world PDCs and snow avalanches³⁶. The frequency f of the most energetic coherent structure in a turbulent flow is given by the Strouhal number Str as

$$Str = f \frac{L}{U} \quad (3)$$

where L and U are the flows' characteristic length- and velocity-scales⁴⁸. For highly turbulent flow conditions with Reynolds numbers $Re > 10^5$, the Strouhal number approaches a constant value of approximately 0.3^{36,49–51}. In our high-Reynolds number experimental PDCs ($Re = 1.5 \times 10^6$), the

measured main frequencies of flow density oscillations of c. 1.26 Hz (i.e., a period of 794 ms) and particle impact rates R of c. 1.33 Hz (a period of 752 ms) coincide closely (Supplementary Fig. 4a and b), and correspond with the period of the visually observed occurrences of the largest flow structures (Fig. 3a–d; Supplementary Fig. 4c). Substituting the experimentally determined frequency $f \sim 1.3$ Hz, the time-averaged height of the gravity current body region $L \sim 1.15$ m and the time-averaged flow velocity $U \sim 4.76$ m s⁻¹ into Eq. (3), gives a Strouhal number $Str = 0.31$ close to the commonly observed value.

The energy peak associated with the most energetic coherent structures, at a frequency of $f \sim 1.3$ Hz, is clearly visible in energy spectra of the total dynamic pressure P_{dyn} , the dynamic pressure of particle impacts $P_{impacts}$ and the dynamic pressure of the continuum dusty gas phase $P_{dusty\ gas}$ at the top of their respective energy cascades (red bars in Fig. 6a–c). The energy of $P_{dusty\ gas}$ decreases strongly with increasing frequency consistent with the transfer of turbulent kinetic energy (per unit volume) to smaller scales of coherent structures (Fig. 6c). By contrast, the energies of $P_{impacts}$ (Fig. 6b) and P_{dyn} (Fig. 6a) show a markedly flatter decay of pressure energy with increasing frequency (and decreasing length-scale of coherent turbulence structure). Importantly, the maximum energy values of both, $P_{impacts}$ and P_{dyn} , which also reach the energy values of the most energetic coherent structures at $f = 1.3$ Hz, occur across a defined band of frequencies f of c. 7–16 Hz (grey bars in Fig. 6a and b). The wavenumbers associated with this frequency band correspond to length-scales of c. 0.25–0.6 m (Fig. 6d and e).

The multiphase origin of dynamic pressure fluctuations

We hypothesize that the origin of the unusually high and temporally clustered dynamic pressures is rooted in the concentration of particles at the peripheries of coherent turbulence structures. PDCs comprise a wide spectrum of particle-gas feedback mechanisms from simple one-way coupling where the motion of particles is affected by the motion of the fluid phase but not vice versa, over two-way coupled particle-gas systems where particle-gas interactions can modify the flow and turbulence structure, to four-way coupling that strongly alters the flow structure⁴. The degree of

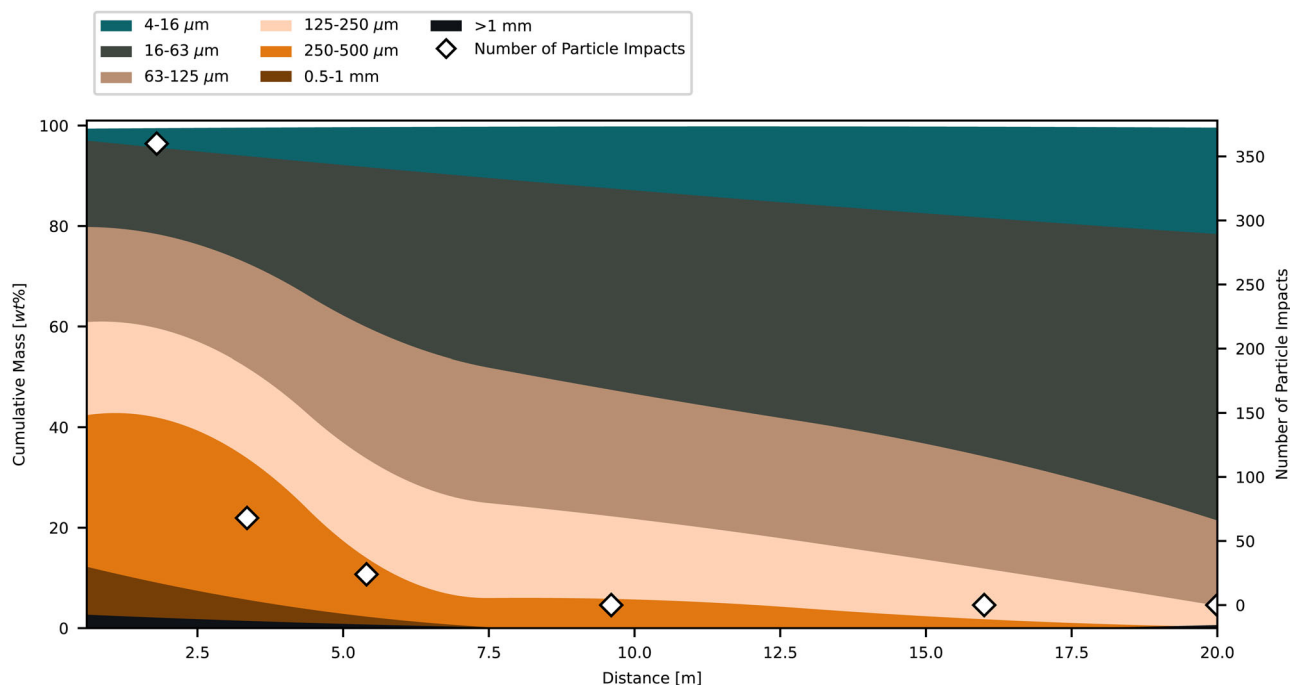


Fig. 4 | Spatial evolution of particle impacts and flow grain-size distribution. The number of particle impacts with the piezoelectric dynamic pressure sensors at mid-flow height (0.45 m from the flow base) as a function of flow distance (white diamond symbols). In comparison, the time-integrated cumulative grain-size distribution of the flow captured in flow samplers at heights of 0.45 m is shown as a

function of flow distance. The decrease of particle impacts with distance follows a similar trend as the decay of particle sizes 125–500 μm in flow samples. Particles with diameters larger than 2 mm (not shown) completely sediment from the flow by c. 1.8 m; particles with diameters >1 mm and >500 μm sediment from the flow at distances of c. 5 m and c. 7.5 m, respectively.

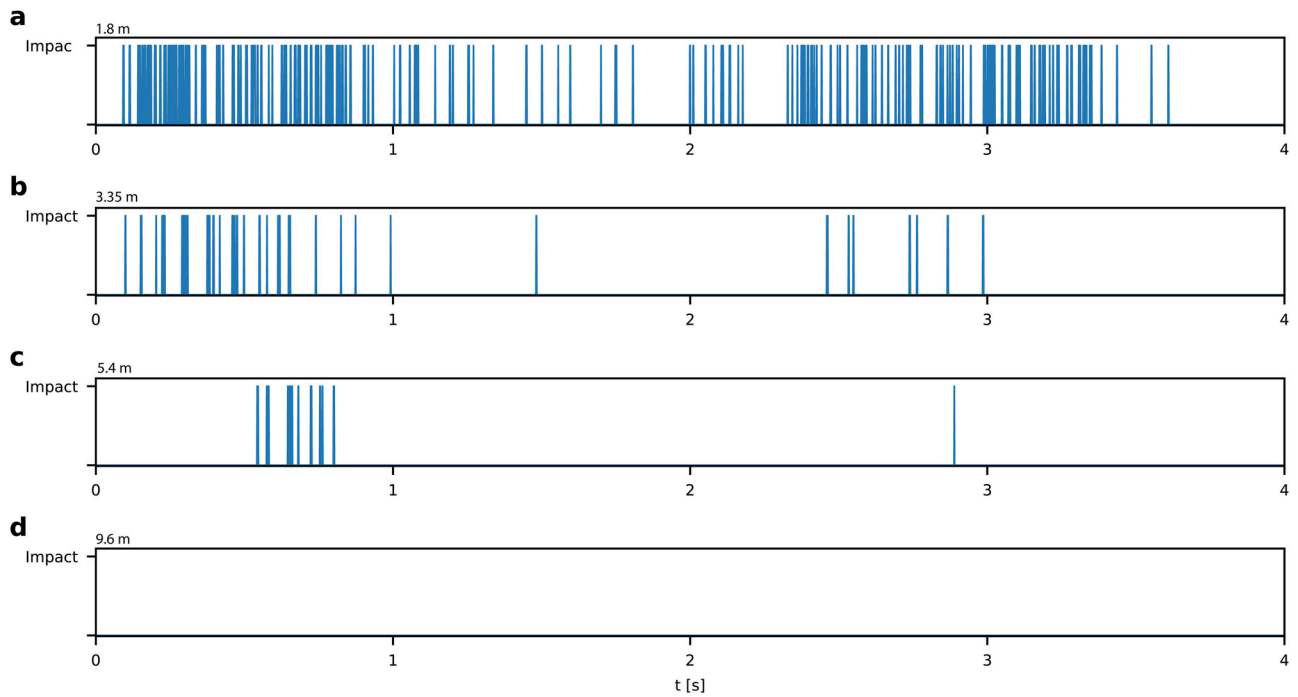


Fig. 5 | Clustered distribution of particle impacts. Timeseries of particle impacts at 0.45 m above the flow base at four different distances from impact: 1.8 m (a), 3.35 m (b), 5.4 m (c) and 9.6 m (d). Occurrences of particle impacts are shown in binary form. That is times of impacts are assigned a value of 1 and times without impacts are assigned a value of zero. The number of particle impacts is strongly decreasing with flow distance and no particle impacts are recorded at the position at 9.6 m. When particle impacts occur, they tend to occur in clusters of several successive impacts. Non-clustered particle impacts are rare. The largest number of particle impacts occur in the head region (c. 0–1 s) and in the mid-body region (c. 2.4–3 s) of the experimental PDC.

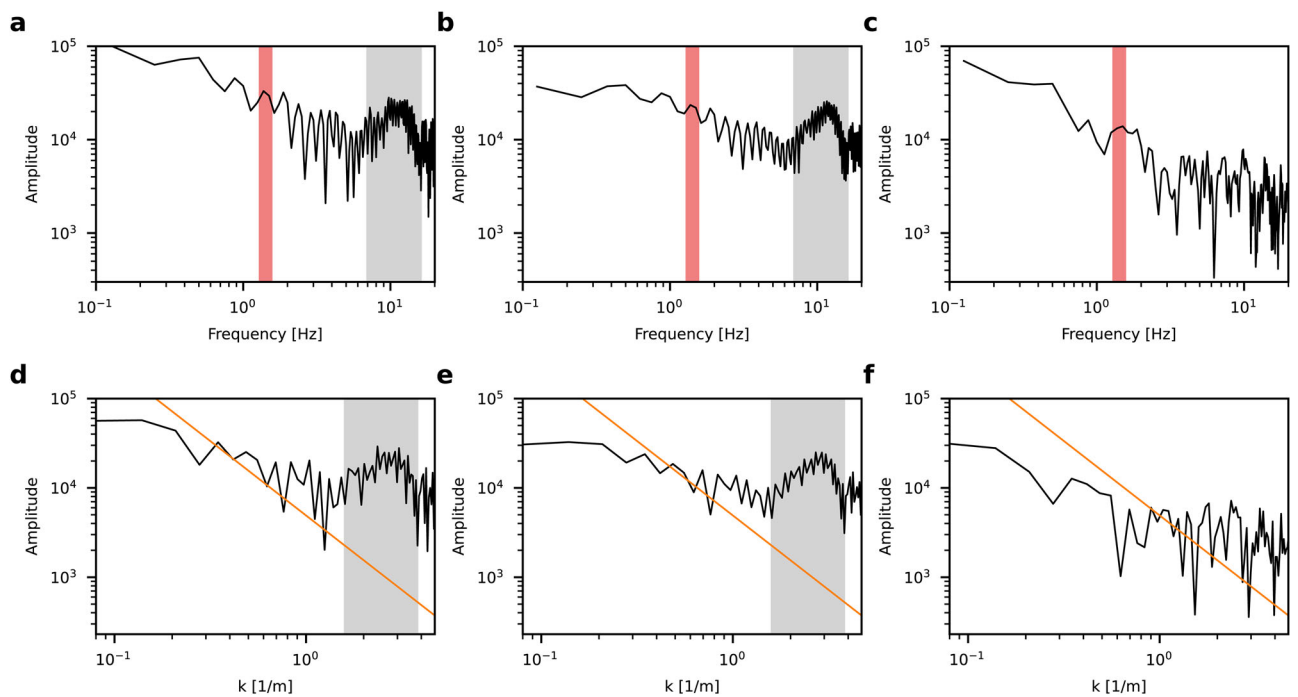


Fig. 6 | Energy spectra of dynamic pressure in Fourier space. Energy spectra of dynamic pressure against frequency for P_{dyn} (a), P_{impact} (b) and $P_{dusty\ gas}$ (c). Energy peaks at a frequency $f \sim 1.3\text{ Hz}$ associated with the largest coherent structures are highlighted by a red bar. This frequency coincides with the measured frequency of the largest coherent structures $f \sim 1.3\text{ Hz} = \frac{U}{L} Str$, where U and L are the time-averaged velocity and thickness of the density current body region and Str is the Strouhal number. The highest-pressure energies occur in P_{dyn} (a) and P_{impact} (b) across a narrow band of frequencies f_{max} from c. 7–16 Hz (where the frequency range f_{max} was visually handpicked) highlighted by a grey bar. Energy spectra of dynamic pressure against wavenumber k for P_{dyn} (d), P_{impact} (e) and $P_{dusty\ gas}$ (f). For P_{dyn} and P_{impact} the high-energy band associated with f_{max} is highlighted by grey bars. This band corresponds to wavenumber of c. $1.6\text{--}4\text{ 1/m}$ or length-scales of coherent structures $1/k$ of c. 0.25–0.6 m. The orange line with slope of $-5/3$ shows the Kolmogorov scaling of the inertial range.

coupling of particles to turbulence structures can be approximated through the particle Stokes number St defined as

$$St = \frac{\tau_p}{\tau_\epsilon}, \tag{4}$$

where τ_p is the characteristic timescale of particles and τ_ϵ is the turbulence timescale. Particles with low Stokes numbers $St \ll 1$ are well coupled with the fluid phase and tend to follow the fluid motion; particles with $St \approx 1$ accumulate at the margins of coherent turbulence structures, while high Stokes number particles $St \gg 1$ are decoupled from fluid turbulence and move independent of the turbulence motion^{25,27,30,48,52,53}. For the condition $St = 1$ of particles concentrating at the peripheries of coherent structures it follows:

$$\tau_p = \tau_\epsilon \Leftrightarrow \tau_p^{-1} = f_\epsilon, \text{ and} \tag{5}$$

$$\Leftrightarrow f_\epsilon = \tau_p^{-1} = \frac{18\rho_F\nu_F F}{\rho_p d^2}, \tag{6}$$

where f_ϵ is the frequency associated with this condition, ρ_F and ρ_p are fluid and particle densities, respectively, ν_F is the kinematic viscosity of the fluid, F is the Stokes drag factor as defined by ref. 54. and d the particle diameter. Equation (6) and our experimental data of the particle size-averaged particle density $\bar{\rho}_p(\bar{d})$ can be combined to calculate the critical frequency $f_\epsilon(d)$ of particle clustering at margins of coherent structures as a function of particle diameter (Fig. 7a). For the polydisperse volcanic mixture used in our experiments (Supplementary Fig. 1), these critical frequencies range over four orders of magnitude from 3×10^{-1} – 4×10^3 Hz. However, the particle sizes associated with the measured energy maximum in $P_{impacts}$ and P_{dyn} at $f_{\epsilon_max} \sim 7$ – 16 Hz (Fig. 5a and b and grey horizontal bar in Fig. 7a),

constitute a narrow band of particle diameters of 117–229 μm (grey vertical bar in Fig. 7a). In flow samples, this particle size range occupies the coarse tail of grainsize distributions (Fig. 7b). Due to sedimentation, the proportion of particles larger than 117 μm strongly decreases from c. 70 wt.% in the initial mixture to <5 wt.% at a flow distance of 20 m (Fig. 4). Similarly, the dynamic pressure energy associated with particle impacts $P_{impacts}$, which, at a runout distance of 1.8 m, accounts for c. 75% of the total dynamic pressure P_{dyn} decreases strongly downstream approximately following a power law decay (Fig. 7c).

The largest particle size supported by turbulence in the experimental flows, which is limited by the characteristic length- and velocity-scales of the most energetic coherent turbulence structure (Eq. (3)) and associated with a measured frequency $f \sim 1.3$ Hz, corresponds to c. 2 millimetres (red vertical bar in Fig. 7a and b). Therefore, the experimental PDC strongly depletes in particles larger than 2 millimetres even before a proper gravity current structure has formed at around 1.8 m after impact. Particle sizes smaller than 2 mm (associated with the frequency of the largest coherent structure), but larger than 117–229 μm (associated with the frequencies at the energy maximum of dynamic pressure f_{ϵ_max} of c. 7–16 Hz) do not form notable peaks in dynamic pressure energy (Fig. 6). This is explained by the rare abundance of particles of this size range, which occupy the coarse tail of flow grainsize distributions (Fig. 7b).

To visualize the process of clustering of particles with critical Stokes numbers at the margins of coherent turbulence structures we conducted a numerical simulation of the experimental PDC using a large eddy resolving, Eulerian-Eulerian approach with particle-fluid four-way coupling. In this multiphase simulation, five different particle sizes are modelled (2 mm, 0.5 mm, 0.125 mm, 0.032 mm and 0.008 mm) whose relative proportions and particle size-dependent densities are the same as in the physical experiment (see Methods for details). Figure 8 depicts contour plots of

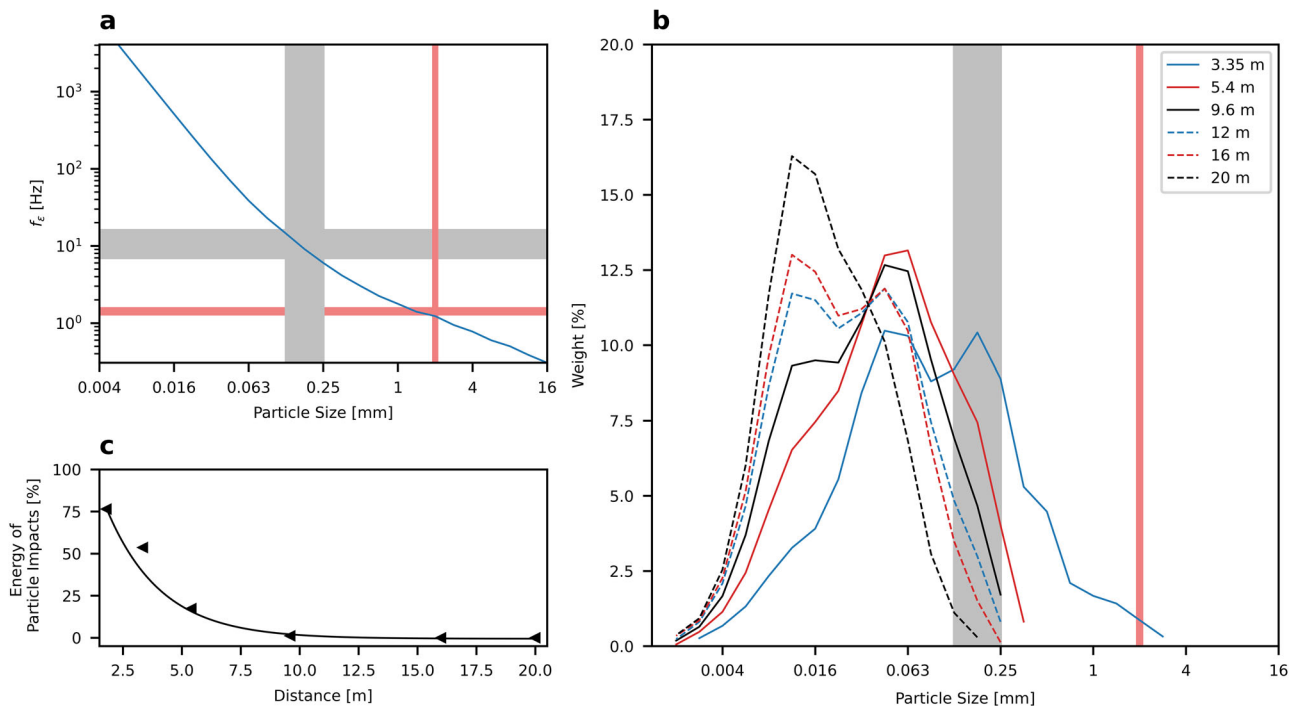
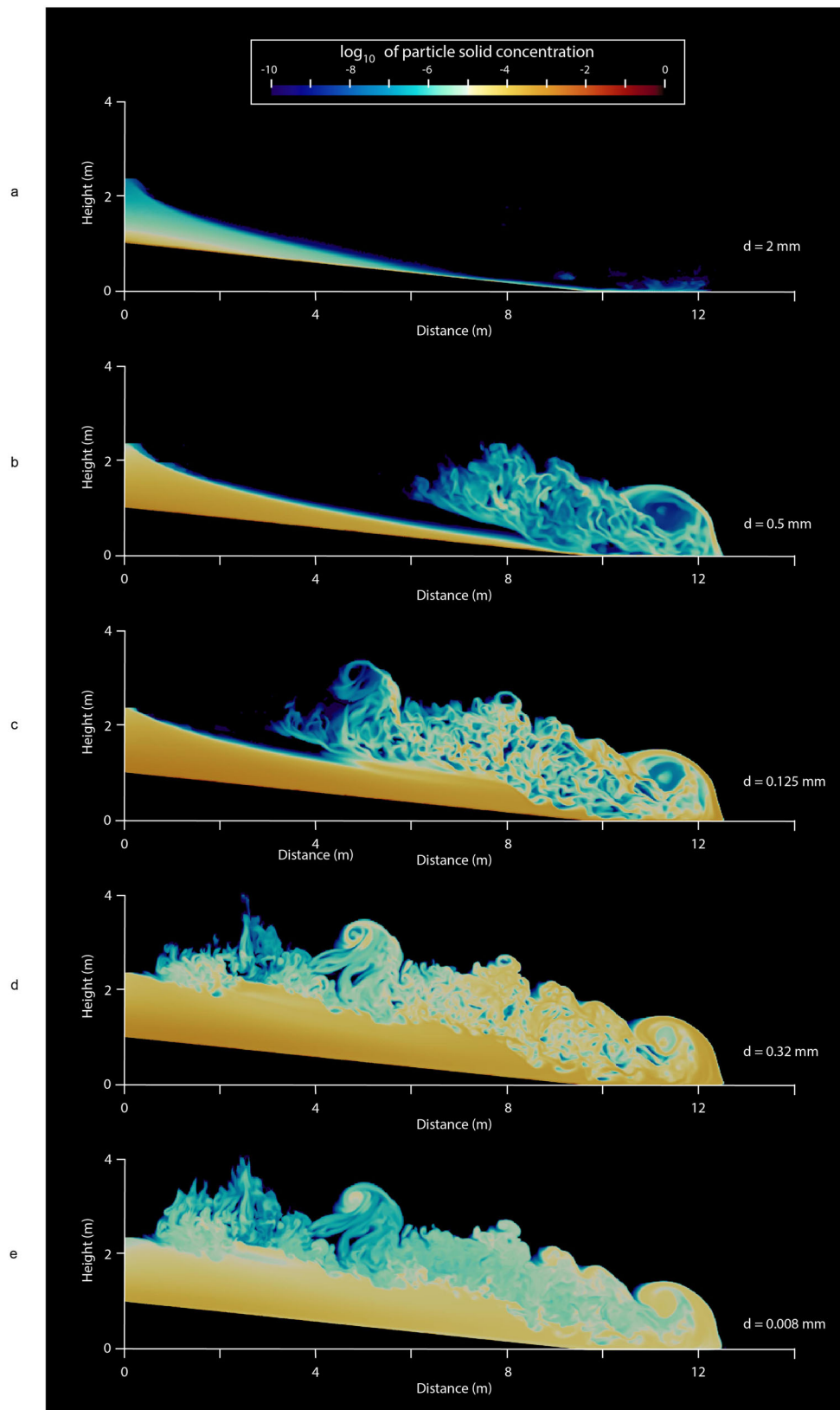


Fig. 7 | Particle sizes of critical Stokes numbers and their sequential sedimentation. **a** The frequency f_ϵ associated with the condition of particle Stokes number $St = 1$ as a function of grainsize. The grey horizontal bar depicts the frequency band in f_ϵ of c. 7–17 Hz of highest-pressure energies. The grey vertical bar delimit the experimentally determined corresponding critical grainsizes for $St = 1$ at f_ϵ of c. 127–224 μm . The red horizontal bar and the red vertical bar mark the frequency associated with the most energetic coherent flow structure at a frequency $f \sim 1.3$ and the corresponding grainsize of c. 2 mm, respectively. **b** Histograms of time-integrated flow grainsize

distributions captured in flow samplers at flow heights of 0.45 m above the flow base for various flow distances. As in ‘a’, the grey vertical bar highlights the grain-size range of c. 127–224 μm associated with f_ϵ , while the red vertical bar marks the critical grainsize of c. 2 mm supported by the most energetic coherent turbulence structures at $f \sim 1.3$. Note the downstream depletion of the flow in critical Stokes number particles associated with f_ϵ (c. 127–224 μm). **c** The fractional time-integrated energy of particle impacts P_{impact} relative to the entire pressure energy P_{dyn} as a function of flow distance. The black line is a best-fit power law to the data.



particle volume concentration of the evolving current at approximately half of the total runout length for each particle size. High Stokes number particles (2 mm in diameter; Fig. 8a) do not highlight any coherent turbulence structures and have sedimented into the basal flow. Low Stokes number particles (0.032 mm and 0.008 mm in diameter; Fig. 8d and e) remain

homogeneously suspended throughout the flow or tend to concentrate slightly in the central regions of coherent structures. By contrast, particles with diameters of 0.5 and 0.125 mm concentrate at the peripheries of eddies highlighting the coherent turbulence structure of the flow (Fig. 8b and c). Similar to our physical experiment, the highest particle concentration in

Fig. 8 | Clustering of critical Stokes number particles at the peripheries of coherent structures. a–e Snapshots from a numerical multiphase Eulerian–Eulerian fluid particle four-way coupled simulation of the physical experiment at approximately mid-flow runout distance. The contour plots show the spatial variation across the simulated PDC in the particle concentration of five modelled grainsizes of 2 mm (a), 500 μm (b), 125 μm (c), 32 μm (d) and 8 μm (e). Technical aspects of the numerical simulation are detailed in the Methods section. Particles with Stokes numbers $St > 1$ (a), which are only supported by turbulence at the scales of the largest

coherent structures, have sedimented into the basal flow and do highlight any coherent structures at mid-flow runout. Particles with critical Stokes numbers $St = 1$ (b and c) concentrate at the peripheries of coherent structures. The effect is stronger for particle sizes of 125 μm than for particle sizes of 500 μm because of the significantly higher abundance of the 125 μm particles over 500 μm particles. Particles with low Stokes numbers $St < 1$ (d and e) tend to be homogeneously suspended or slightly concentrate in the central parts of coherent structures.

eddy peripheries occurs for particles with diameters of 0.125 mm. The average size of the large coherent structures (highlighted by concentrated margins) in the numerical simulation accounts to approximately 0.5 m (Fig. 8c). This corresponds to the length-scales of c. 0.25–0.6 m that are associated with the narrow band of maxima in dynamic pressure as seen in the energy spectra of dynamic pressure as a function of wavenumber (where the length-scale is the inverse of the wavenumber k ; Fig. 6d and e).

Spatiotemporal evolution of dynamic pressure fluctuations

To assess the destruction potential of PDCs, volcanologists routinely use estimates of either bulk flow or local time-averaged flow velocity and density values to evaluate average dynamic pressures^{26,41–43}. Our finding of the concentration of particles with critical Stokes numbers (i.e., $St = \mathcal{O}(1)$) at the peripheries of coherent turbulence structures imply strong fluctuations of dynamic pressure to occur at the characteristic frequency $f_{\epsilon_{\max}}$ of these structures. To prevent underestimation of the destruction potential of PDCs, it is important to understand how turbulent fluctuations of dynamic pressure around field-estimated average values evolve during flow propagation.

Figure 9a compares the time-averaged dynamic pressure $P_{dusty\ gas_ave}$, the maximum dynamic pressure of the continuum phase $P_{dusty\ gas_max}$ and the maximum dynamic pressure associated with particle impacts $P_{impact\ max}$ as a function of flow distance. $P_{dusty\ gas_ave}$ (i.e., the equivalent of the time-averaged pressure estimated in hazard assessments to assess damage to infrastructure) steadily decreases with flow distance D following a powerlaw of the form $P_{dusty\ gas_ave} \propto 1/D$. By contrast, and up to 9.6 m, the maximum loading pressure $P_{dusty\ gas_max}$ exceeds the time-averaged pressure by an order of magnitude. In distal reaches, $D > 9.6$ m, $P_{dusty\ gas_max}$ starts to decline more strongly. Maximum dynamic pressures from particle impacts $P_{impact\ max}$ exceed $P_{dusty\ gas_ave}$ by two orders of magnitude, strongly decline with distance and are restricted to the proximal flow reaches of $D \leq 5.4$ m.

Figure 9b shows the pressure ratio of $P_{dusty\ gas_max}$ over $P_{dusty\ gas_ave}$ against flow distance. This ratio assesses by how much current field-based estimates of dynamic pressure underestimate actual, turbulence-enforced maximum loading pressures and can be written as:

$$\frac{P_{dusty\ gas_max}}{P_{dusty\ gas_ave}} = \frac{\rho_{\max} U_{\max}^2}{\rho_{ave} U_{ave}^2}. \quad (7)$$

The pressure ratio is independent of scale, and experimental estimates can be applied to natural flow scales. However, the spatiotemporal evolution of the dynamic pressure ratio is limited by the abundance of large Stokes number particles inside flows. Following the decoupling of high Stokes number particles from the margins of coherent structures, their motion is independent of fluid turbulence and results in their rapid sedimentation from the flow.

Immediately following formation of a gravity current structure at c. 1.8 m and up to 5.4 m, the pressure ratio continuously increases from initial values of c. 11.8 to maxima of c. 13 in 0.74 s (Fig. 9b). This duration coincides with the characteristic eddy timescale of the largest coherent structure of $\tau_{\epsilon} = 1/f \sim 1/1.3 = 0.77$ s. This suggests that the characteristic timescale of the motion of high Stokes number particles from a homogeneous suspension into eddy peripheries can be estimated by the overturn time of the largest coherent structure.

After the time τ_{ϵ} , the particle volume fraction θ_V of particles with $St = \mathcal{O}(1)$ declines below 10^{-4} . This appears to correspond to the limiting mass loading for maximum particle clustering to occur and, downstream of 5.4 m, the pressure ratio decreases strongly. At 20 m, where the volume fraction of particles with $St = \mathcal{O}(1)$ has decreased to values of $\theta_V \sim 5 \times 10^{-6}$, the pressure ratio approaches a value of 3.84. In the case of exhaustion of $St \sim 1$ particles carried inside flows, Eq. (7) reduces to:

$$\frac{P_{dusty\ gas_max}}{P_{dusty\ gas_ave}} \sim \left(\frac{U_{\max}}{U_{ave}} \right)^4 \quad (8)$$

(see Supplementary note 2). Our velocity measurement of the maximum and average velocity at 20 m give a value of $(U_{\max}/U_{ave})^4$ of 3.9 in Eq. 8, which closely corresponds with the measured pressure ratio of 3.84.

Discussion

Current approaches to assess the destruction potential of pyroclastic density currents envisage the loading force of a continuum multiphase fluid of characteristic velocity and density across structural surfaces opposing flow direction.^{37–40} In the absence of detailed measurements inside flows, volcanologists estimate local time-averaged values of flow velocity and density from deposit or damage characteristics to guide assessments of potential hazard impact^{15,41–43}. Our simulations of pyroclastic density currents through large-scale physical experiments and numerical modelling demonstrate a fundamental shortcoming of this approach: the modification of the flow and turbulence structure due to coupled feedbacks between particle and gas phases. This feedback leads to the preferential clustering of large, high-momentum particles at the margins of coherent turbulence structures (Fig. 10a) and generate two different types of distinct hazard impacts (Fig. 10b–c).

The first type, the dynamic pressure of the continuous dusty gas phase $P_{dusty\ gas}$, significantly exceeds the time-integrated dynamic pressure by up to one order of magnitude (Fig. 10d). The cause of these strong turbulent pressure fluctuations is the modification of the flow into coherent structures with high-density margins (Fig. 10a), spatially separating the flow into high density (eddy peripheries) and lower density domains (central regions of eddies). The size of the coherent structures, and hence the characteristic frequency of high-density/high dynamic pressure flow pulsing $f_{\epsilon_{\max}}$, is determined by the abundance of particles whose characteristic response time to fluid motion is equal to or smaller than the characteristic time-scale of changes in the fluid motion (that is, particle Stokes numbers $St \geq 1$). Depending on the mass loading of particles with this critical Stokes number condition, the ratio of the clustering-enforced maximum dynamic pressure $P_{dusty\ gas}$ and the field-estimated average pressure can range between c. 4–13. To prevent an underestimation of the intensity of hazard impact, we strongly suggest that these factors are applied to conventional estimates of dynamic pressure that apply bulk flow values of flow velocity and density^{15,41–43}. For instance, for two- to three-story, reinforced brick, stone and concrete buildings, a mean dynamic pressure of 5 kPa results in failure of doors and partial damage to door and window frames. By comparison, 4–13 times larger maximum clustering-enforced dynamic pressures of 20–65 kPa lead to failure of peaked roofs and front-facing exterior walls (c. 20 kPa) and complete failure of all building elements (c. 65 kPa)¹⁵. Oscillation in dynamic pressure at the frequency $f_{\epsilon_{\max}}$ further intensifies the destructiveness of flows due to the progressive structural weakening of

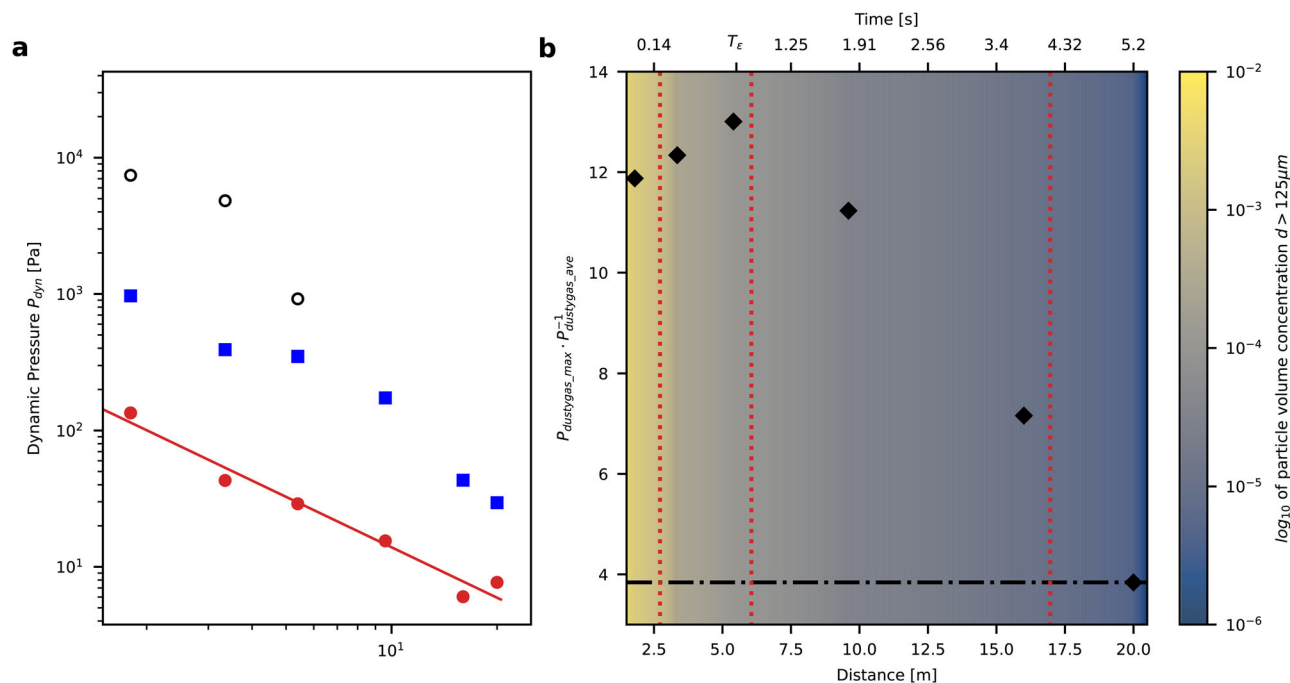


Fig. 9 | Spatiotemporal evolution of dynamic pressure during flow propagation. **a** Dynamic pressure as a function of flow distance D . The red circles show time-averaged values of dynamic pressure $P_{dust\ gas_ave}$. The red line is a best-fit powerlaw through the data that yields $P_{dust\ gas_ave} = 136D^{-1.019}$. The blue square symbols represent the maximum dusty gas pressure $P_{dust\ gas_max}$. The black circles show measurements of the maximum particle impact pressure P_{impact_max} . **b** The pressure ratio $P_{dust\ gas_max}/P_{dust\ gas_ave}$ as a function of flow distance (black diamonds). The contour plot shows the particle volume concentration of particles with diameters $>125\ \mu\text{m}$, associated with the condition $St \geq O(1)$. The vertical red dotted lines demark particle concentrations of, from left to right, 10^{-3} , 10^{-4} , and 10^{-5} .

The secondary, non-linear horizontal time axis depicts the times of flow front arrival corresponding to these distances. After formation of a gravity current structure at c. 1.8 m and up until 5.4 m, the pressure ratio increases slightly to maximum values of around 13. The flow duration associated with this increase coincides with the eddy time scale t_ϵ highlighted on the secondary x-axis. Downstream from 5.4 m, the pressure ratio decreases in association with a reduction in the particle concentration of critical Stokes number particles larger than $125\ \mu\text{m}$. The horizontal dashed line corresponds to the condition predicted by Eq. (8) where the pressure ratio takes a critical value of c. 3.9, when the flow is depleted in particles with $St \geq 1$.

materials amid repeated high-pressure loading. The damage inflicted depends on the maximum dynamic pressure associated with the high-density margins of coherent turbulence structures and the characteristic integral length scale of these structures relative the characteristic length scale of an infrastructure. Our experimental method does not allow us to determine the range of three-dimensional geometries of coherent turbulence structures and future physical and numerical experiments are needed to address this problem. However, our experimental results can give some guidance. The characteristic length scale of the most energetic turbulence structures with particle clusters of c. 0.25–0.6 m is of the order of the height of the lower flow boundary to roughly half of the thickness of the body the density current. This length scale (i.e. half the thickness of the PDC) is considerably larger than the height of the common built environment at the Earth’s surface. Limited by the mass loading of particles with particle Stokes numbers of order unity in a PDC, this indicates that clustering-enforced destructiveness will be effective in typical PDC/infrastructure interactions. The modification of the flow and flow turbulence structure through particle-gas feedback also implies associated modifications of the local concentration of readily respirable fine-ash particles and local flow temperature, with effects on the respiratory and burns hazards of PDCs.

The second type of hazard impact, the force of particle collisions, which is associated with (and measured in our experiments as) the dynamic pressure of particle impacts P_{impact} can exceed average dynamic pressures, even stronger than $P_{dust\ gas}$, by two orders of magnitude (Fig. 10d). Unlike a loading continuum pressure, this pressure corresponding to the force of particle impacts results when particles with Stokes numbers $St \geq 1$ uncouple from the flow that engulfs a structure and directly impinge onto it. The resulting piercing particle impacts can be seen as pockmarks on trees and infrastructure⁵⁵ (Fig. 10c) and are illustrated for the case of the Merapi 2010

eruption in Supplementary Fig. 5. Piercing particle impacts from PDCs are also likely contributing to the failure of brittle structures such as glass windows^{38,55}. Importantly, the magnitude of particle impact forces, because they are distributed over relatively small impact areas of the order of the cross-sectional area of a particle, must be considered as a potential contributor to the high fatality and injury rates in PDC-forming eruptions (Fig. 10d).

Our experiments demonstrate the role of turbulent particle-gas feedback in modifying the flow and turbulence structure and exacerbating the intensities of hazard impacts. These findings are also applicable to other types of high-Reynolds number, polydisperse particle-gas flows, such as powder snow avalanches, dust storms, and the debris-laden basal flow regions of tornados and explosions, and should be considered in the assessments of their potential hazard impacts^{28,56–59}.

Methods

Large-scale experiments

The Pyroclastic flow Eruption Large-scale Experiment (PELE), which is fully described in ref. 44., is an international test facility to synthesize, view and measure inside the interior of pyroclastic density currents. Experimental PDCs of up to six tonnes of volcanic material and gas move at velocities of $7\text{--}32\ \text{m s}^{-1}$, are 2–4.5 m thick and propagate to runout length of $>35\ \text{m}$. We conducted a series of three large-scale experiments to confirm that the experimental results reported are typical. The currents are generated by the controlled gravitational collapse of variably diluted suspensions of pyroclastic particles and gas from an elevated hopper into an instrumented runout section. PELE is operated inside a 16 m high, 25 m long and 18 m wide disused boiler house. The apparatus is composed of four main structural components: (i) Tower. A 13 m-high construct that lifts either a $4.2\ \text{m}^3$

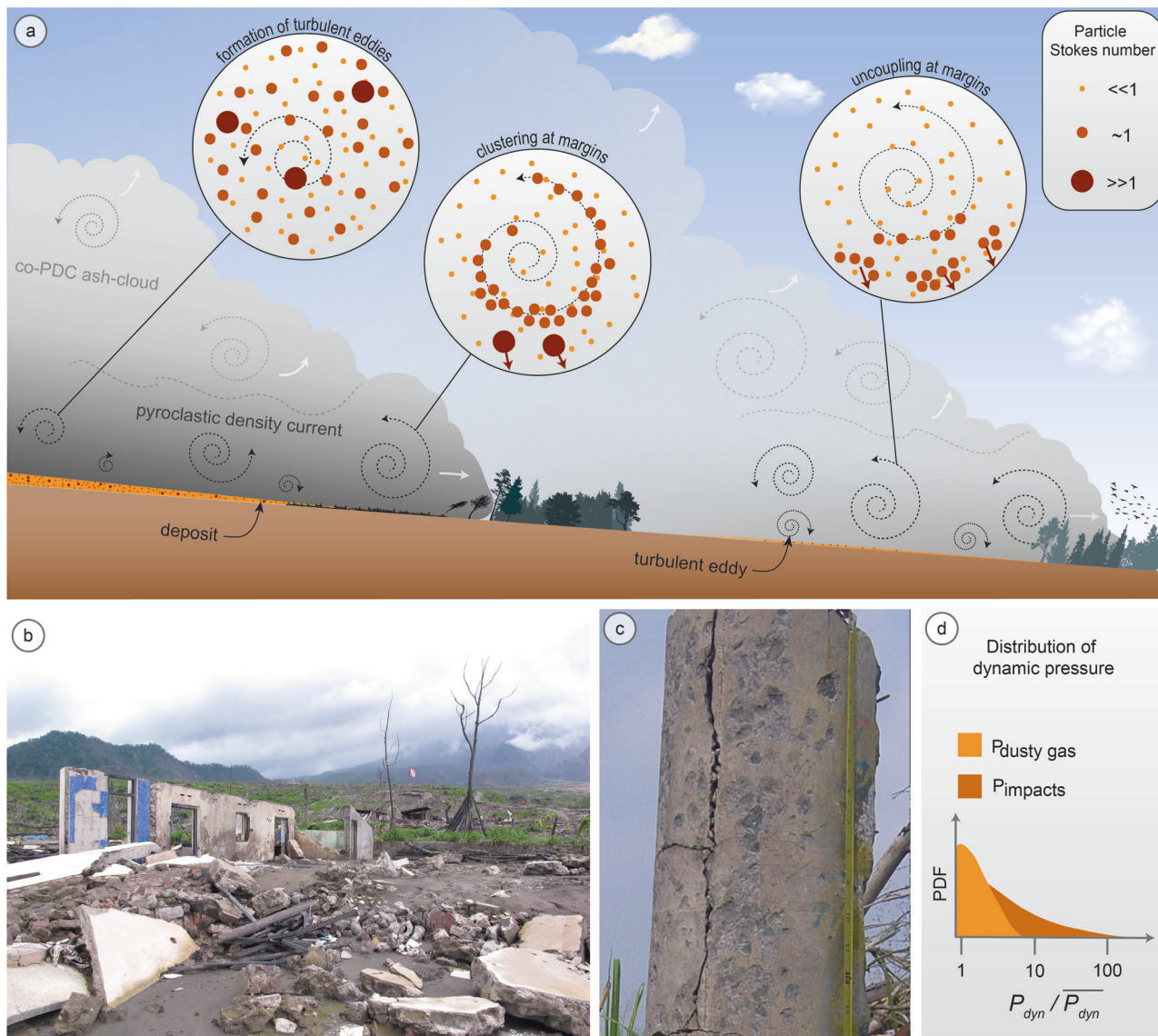


Fig. 10 | The effects of gas-particle feedbacks on pyroclastic density current hazards. **a** Schematic presentation of the processes of turbulent gas-particle feedback in PDCs at the scale of an idealized eddy at three different times. For the polydisperse multiphase flow, the spectrum of concurrent behaviours of particles with different degrees of coupling to turbulent fluid motion is illustrated for particles with three different particle Stokes numbers St . *Left eddy*: initial stage where all particles are homogeneously dispersed. *Middle eddy*: intermediate stage, after the overturn time of the largest coherent turbulence structure. $St \sim 1$ particles preferentially cluster on eddy margins, while $St \ll 1$ particles remain homogeneously dispersed following turbulence motion and $St \gg 1$ particles move unhindered by turbulence. *Right eddy*: later stage, when clusters of dominantly $St \sim 1$ particles

decouple from eddy margins and sediment as mesoscale turbulence clusters. **b** Example of the damage effects of clustering-enforced dynamic loading pressure $P_{dusty\ gas}$ as repeated high-pressure impacts at the frequency $f_{\epsilon-max}$. **c** Example of the piercing damage effects of the direct impact of high St particles or particle clusters with structures generating pockmarks on the upstream face of a concrete pole. **d** Schematic probability density function of dynamic pressure P_{dyn} relative to the average dynamic pressure $\overline{P_{dyn}}$ concurrently considered in hazard assessments. The dynamic pressure of the continuum dusty gas phase $P_{dusty\ gas}$ exceeds the average pressure by one order of magnitude. The dynamic pressure associated with particle impacts P_{impact} exceeds the average dynamic pressure by two orders of magnitude.

hopper (for moderate to high discharge rates of $300\text{--}1,500\text{ kg s}^{-1}$) or a 0.7 m^3 hopper (for discharge rates of $30\text{--}200\text{ kg s}^{-1}$) to the desired discharge height. The hoppers are equipped with internal hopper heating units to heat the pyroclastic material to target temperatures of up to $400\text{ }^\circ\text{C}$. The heating process is measured by thermocouples and the hopper is mounted onto four load cells to capture the time-variant mass discharge. (ii) Column. A $\leq 9\text{ m}$ high shroud of heat-resistant cloth through which the discharge particle-air mixtures accelerate under gravity. (iii) Chute. A 17 m long and 0.5 m wide multi-instrumented channel section with $0.6\text{--}1.8\text{ m}$ high sides of temperature-resistant glass. The first 12 m are variable adjustable to slope angle between 5° and 25° while last 5 m of the channel is horizontal. (iv) Outflow. A 25 m -long flat instrumented and unconfined runoff section

that extends outside the building. The physical properties of the particle-gas suspensions prior to impact with the channel (velocity, mass flux, volume flux, particle concentration), the characteristics of the solid components (grainsize distribution, particle density distribution, particle temperature), and boundary conditions (substrate roughness, chute slope and channel width) can be modified to generate a wide range of reproducible natural flow conditions⁴⁴. For the experiments reported in this study, we used the small hopper of 0.7 m^3 to generate fully turbulent experimental PDCs with a basal bedload region, but without a dense basal underflow, which would form at the high discharge rates in the large hopper setup condition.

The use of pyroclastic solids material and air is an important prerequisite to generate natural stress coupling between the fluid and solid

phases. The pyroclastic material, containing particle sizes from 2 μm to 16 mm, consists of a mixture of two well-characterized ignimbrite deposits F1 and F2 from the 232 CE Taupo eruption⁴⁷. The first component (F1) is a proximal medium-ash-dominated ignimbrite deposit with a unimodal grain-size distribution, a median diameter of 366 μm, and 4.5 wt.% of extremely fine ash (<63 μm). The second component (F2) is a fine ash rich facies from the base of the proximal Taupo ignimbrite deposit with a polymodal grain-size distribution, a median diameter of 103 μm, and 36.5 wt.% of extremely fine ash. The experiments reported in this study involve a material blend with F1 = 60 wt.% and F2 = 40 wt.% (the grain-size distribution is shown in Supplementary Fig. 2a) yielding a mixture with 20 wt.% of particles smaller than 63 μm. The main solids components of the pyroclastic material are highly vesicular pumice, glass shards, free crystals and lithic particles. The relative proportion of these components vary with grain-size. The average particle density as a function of particle diameter is shown in Supplementary Fig. 2b.

The resulting experimental pyroclastic density currents are fully turbulent with Reynolds numbers in the lower 10⁶ (and up to 10⁷ in proximal regions). Dimensionless products quantifying the scaling similarity of natural and experimental currents for the bulk flow are depicted in Supplementary Table 1. Further details of the experimental protocol, properties of the volcanic material, and measurement techniques are reported in ref. 44, but the measurements and analytical methods specific to the results presented here are detailed below.

Sensors and analytical methods

Twenty fast cameras (60–120 frames per second) and three normal-speed cameras (24–30 frames per second) positioned at different distances and viewing angles, recorded the downstream propagation of the experimental pyroclastic density currents. At flow distances of 1.8 m, 3.35 m, 5.4 m, and 9.6 m, four highspeed camera profiles consisting of six highspeed cameras recorded vertical profiles of the passing flows at 500 frames per second. LED floodlight arrays were used to achieve sufficient and even illumination, which allowed for a detailed analysis of the gas-particle transport and sedimentation with particle image analysis (PIV; using the algorithm PIVlab⁶⁰). Two-dimensional velocity fields were derived with PIV from the highspeed videos at time intervals of 2 ms.

Timeseries of dynamic pressure $P_{dyn}(t)$ were measured with piezoelectric pressure sensors (PCB Piezotronics 106B51 and signal conditioners PCB 483 C) at the flow centerline, at flow distances of 1.8 m, 3.35 m, 5.4 m, 9.6 m, 16 m, and 20 m from impact and were recorded at a sampling rate of 1 kHz. The sensors consist of a quartz crystal encapsulated in a solid steel casing. The deformation of the steel casing due to pressure variations is transferred to the quartz crystal, which induces a voltage that is directly recorded as calibrated dynamic pressure signal. In our experiments, we exposed only the frontal face of the sensor to the flow. This frontal face is covered by a circular, 15.7 mm diameter, frontal steel diaphragm. The sensors were mounted into 0.1 m-long bullet-shaped sensor mounts to reduce flow separation at the upstream-directed sensor head. The encased pressure sensors protruded out of 1.8 m-high wing-shaped profiles designed to reduce flow separation behind the profiles and to guide cabling. In this study, we report the results of dynamic pressure measurements obtained at approximately the mid-depth of the density current body region at a slope-normal height $z = 0.45$ m above the flow base. Supplementary Note 1 and Supplementary Fig. 3 show a comparison of the measured dynamic pressure signals due to the forces of impacts of individual particles with the sensor with theoretical estimates of impact pressures for the cases of purely elastic and purely inelastic collisions. For the case of inelastic particle collisions, the particle collision time is given by the ratio of the diameter of the particle colliding with the sensor and the velocity of impact. Due to the fast response time of the dynamic pressure sensors of 12 μs and taking a typical flow velocity of 8 ms⁻¹ as reference, collisions of particles larger than c. 100 μm can be detected in our experiments.

To test the sensor response to particle impacts, we conducted additional laboratory-scale experiments using a particle gun and spherical glass

beads with three different ranges in particle diameter. The particle gun consists of a 1 m long, 0.01 m diameter steel pipe connected to a compressed air line. The air velocity was regulated through an inlet air-pressure valve and the gas velocity was measured with a hotwire anemometer. A funnel system in the particle gun allows the feeding of individual particles and mixtures of particles into the airstream. The dynamic pressure sensor was positioned 2 cm in front of the particle gun. Collision experiments were performed with individual, spherical glass bead particles with particle diameters of 170–180 μm, 300–355 μm and 400 μm and the pressure signal was recorded at the same sampling rate of 1 kHz as in the large-scale experiments. Particles were fed into the particle gun when the transient signal of the piezoelectric dynamic pressure sensor due to the dynamic pressure of the airflow had decayed to a zero Pascal baseline. This allowed an analysis of the recorded dynamic pressure signal associated with the impact force of a particle colliding with the sensor without removing the component of dynamic pressure corresponding to the air flow alone.

As detailed in Supplementary Note 1 and Supplementary Fig. 3, the signals of dynamic pressure recorded by the dynamic pressure sensors due to the force of a particle colliding with the sensor diaphragm is the impact force distributed over the surface area of the particle impact (i.e. the cross-sectional area of the particle). This is different from a piezoelectric force sensor where the force is distributed over the entire surface of the sensor head. In Supplementary Note 1 and Supplementary Fig. 3 it is also shown that the particle collisions with the dynamic pressure sensor are close to and well approximated as purely inelastic collisions.

At flow distances of 0.5 m, 1.8 m, 3.35 m, 5.4 m, 9.6 m, 12 m, 16 m, and 20 m from impact vertical arrays of transparent sediment samplers collected the flowing mixture. During the experiment, the sequential filling the flow samplers was filmed with highspeed cameras. These samplers are open on the upstream side allowing the flow to enter through the 1.69 cm² cross-sectional area while on the downstream side, a 16 microns mesh allows only the gas-phase of the flow to exit, leading to accumulation of the transported particles inside the sampler. From this we measure continuous data of flow sediment passing a position as a function of time. Downslope velocity components $u(t)$ of the flow at a position 5 cm upstream of each flow sampler were obtained through PIV. The weight and density of the material deposited inside the flow samplers was measured at selected time intervals to calculate the time-variant porosity of the captured sediment, as well as the sediment grain-size distribution. Particle solids-concentration C_s are defined as

$$C_s(z, t) = \frac{V_d(1 - \varepsilon)}{u A_o t} \quad (9)$$

where V_d is the time-variant sediment accumulated volume inside the flow sampler, u is the time-variant downslope velocity obtained through PIV at the entrance of the flow sampler, A_o is the cross-sectional area of the flow sampler, t the selected time intervals, ε the time-variant sediment porosity, and z the height in slope-perpendicular direction.

At each of the flow sampler locations, time-variant and height-variant temperature $T(z, t)$ is measured in vertical arrays of fast thermocouples (410–345 Type K) with a sampling rate of 70 Hz. The response time of the thermocouples is approximately 1 millisecond and hence faster than the sampling rate. Together with the time-series of time-variant and height-variant flow velocity $u(z, t)$, grain-size distributions, volumetric particle concentrations $C_s(z, t)$, the temperature time-series allow for the calculation of dynamic pressure $P_{dyn_Bernoulli}$ defined by Eq. (1) where bulk flow density $\rho_C(z, t)$ is given by

$$\rho_C = C_s \rho_p + \frac{P_a}{\gamma_g R_g T} (1 - C_s) \quad (10)$$

where ρ_p is the particle density, P_a is the ambient pressure, γ_g is the mass fraction of the gas components (including moisture) and R_g is their gas constants.

Energy spectra

For the computation of discrete Fourier spectra, the NumPy FFT function of ref. 61. is used. From the complex output provided by the FFT functions only the real part is used. Due to the symmetry of the Fourier transform and physical meaning only positive frequencies are considered.

For the calculation of wave numbers, the time axis (t) of the data is transferred into advected distances (x) by multiplication with time averaged velocities ($x = \bar{u} \cdot t$). Using the data series as function of advected distance, Fourier transforms are calculated using the NumPy implementation. Also, for these spectra only the real and positive part of the output is used.

Multiphase flow simulation of the PELE experiments

Numerical simulations using the Eulerian–Eulerian approach, also known as the two-fluid method (TFM), were performed to reproduce the experimental currents. We employed the open-source Multiphase Flow with Interphase eXchanges (MFIx) solver, developed by the National Energy Technology Laboratory (NETL) within the US Department of Energy. This technique enables us to solve mass, momentum, and energy equations for both fluid and solid phases, capturing solid–fluid 4-way coupling. A comprehensive description of all equations can be found in ref. 62.

We executed the 3D flow simulation on the ARCHER2 cluster utilizing 1200 CPU cores with 3 Tb of RAM for 15 days, employing the large-eddy-simulations (LES) with the wall-adapting local eddy-viscosity subgrid model WALE of ref. 63. to model subgrid turbulence. The initial and boundary conditions for the simulations were established based on the international benchmarking and validation exercise for PDC model⁶⁴.

The top boundary of the domain is described as a pressure boundary that creates a stratified “atmosphere”. All other boundaries, except the inlet, follow the no-slip boundaries for the fluid phase and partial slip for the solid phase, following the work of ref. 65. The experimental geometry was uploaded in MFIx as an STL file upon which we created a roughness of approximately 0.01 m in height to emulate the basal boundary conditions. The mesh was cut to follow the geometry using the cutcell method⁶².

The inlet boundary is treated as a mass inflow, where a flux of temperature, fluid and solid concentration and velocity were prescribed. The continuous grain-size distributions of the experimental mixture was discretized in five bins of particles with a diameter of 2×10^{-3} m, 5×10^{-4} m, 125×10^{-6} m, 32×10^{-6} m and 8×10^{-6} m. This representation preserves the mean size diameter $D[3,2]$ (surface-mean diameter) and $D[4,3]$ (volume-mean diameter) consistent with the experimental counterpart. We also discretized the solid density distribution into the same respective five bins to ensure accurate gas-particle coupling in the simulation. In order to match experiments closely, the inlet used time- and height-variant velocity, concentration, grain-size distribution and temperature profiles described by ref. 66.

At the inlet, we assumed thermal and kinetic equilibria, resulting in uniform temperature and no-slip velocity across all phases in each inlet computational cell. However, the numerical simulation captured thermal and kinetic decoupling, dictated by particle Stokes number as shown in Fig. 8. Using the finite volume method with a second-order solver and Superbee limiter, the MFIx solves mass, momentum and energy equations. This approach allows us to derive the temperature, velocity, and concentration fields for the fluid and each solid phase in each computation cell. The results were saved as binary VTK files, which were loaded in Paraview[®] v5.11 using the Talapas HPC at the University of Oregon and subsequently exported as images. The input and boundary conditions used in the simulations are summarized in Supplementary table 2.

Data availability

The data generated in this study are available at <https://doi.org/10.5281/zenodo.10725051>.

Code availability

The code used to produce the data analyses of the experimental data is freely available at <https://www.python.org>. The code used to conduct the large-eddy

resolving multiphase simulation is freely available at <https://mfix.netl.doe.gov/products/mfix/>.

Received: 20 October 2023; Accepted: 4 March 2024;

Published online: 09 May 2024

References

- Neri, A., Esposti Ongaro, T., Voight, B. & Widiwijayanti, C. Pyroclastic Density Current Hazards and Risk, in: Papale, P., Shroder, J. (Eds.), *Volcanic Hazards, Risks and Disasters*. Elsevier Science (2014).
- Dufek, J., Esposti Ongaro, T. & Roche, O. Pyroclastic Density Currents: Processes and Models, in Sigurdsson et al. (Eds.) *Encyclopedia of Volcanoes*, 2nd Ed., pp 617–629 (2015).
- Sulpizio, R., Dellino, P., Doronzo, D. M. & Sarocchi, D. Pyroclastic density currents: state of the art and perspectives. *J. Volcanol. Geotherm. Res.* **283**, 36–65 (2014).
- Lube, G., Breard, E. C. P., Esposti-Ongaro, T., Dufek, J. & Brand, B. Multiphase flow behaviour and hazard prediction of pyroclastic density currents. *Nat. Rev. Earth Environ.* **1**, 348–365 (2020).
- Dufek, J. The fluid mechanics of pyroclastic density currents. *Ann. Rev. Fluid Mech.* **48**, 459–485 (2016).
- Chester, D., Degg, M., Duncan, A. & Guest, J. The increasing exposure of cities to the effects of volcanic eruptions: a global survey. *Glob. Environ. Change B: Environ. Hazards* **2**, 89–103 (2000).
- Small, C. & Naumann, T. The global distribution of human population and recent volcanism. *Environ. Hazards* **3**, 93–109 (2001).
- Auker, M. R., Sparks, R. S. J., Siebert, L., Crossweller, H. S. & Ewert, J. A statistical analysis of the global historical volcanic fatalities record. *J. Appl. Volcanol.* **2**, 2 (2013).
- Valentine, G. A. Stratified flow in pyroclastic surges. *Bull. Volcanol.* **49**, 616–630 (1987).
- Lube, G. et al. Kinematic characteristics of pyroclastic density currents at Merapi and controls of their avulsion from natural and engineered channels. *Geol. Soc. Am. Bull.* **123**, 1127–1140 (2011).
- Lube, G. et al. Dynamics of surges generated by hydrothermal blasts during the 6 August 2012 Te Maari eruption, Mt. Tongariro, New Zealand. *J. Volcanol. Geotherm. Res.* **286**, 348–366 (2014).
- Cronin, S. J. et al. Insights into the October–November 2010 Gunung Merapi eruption (Central Java, Indonesia) from the stratigraphy, volume and characteristics of its pyroclastic deposits. *J. Volcanol. Geotherm. Res.* **261**, 244–259 (2013).
- Charbonnier, S. J. et al. Unravelling the dynamics and hazards of the June 3rd, 2018, pyroclastic density currents at Fuego volcano (Guatemala). *J. Volcanol. Geotherm. Res.* **436**, 107791 (2023).
- Huppert, H. E. & Simpson, J. E. The slumping of gravity currents. *J. Fluid Mech.* **99**, 785–799 (1980).
- Valentine, G. A. Damage to structures by pyroclastic flows and surges, inferred from nuclear weapons effects. *J. Volcanol. Geotherm. Res.* **87**, 117–140 (1998).
- Andrews, B. J. & Manga, M. Effects of topography on pyroclastic density current runout and formation of co-ignimbrites. *Geology* **39**, 1099–1102 (2011).
- Andrews, B. J. & Manga, M. Experimental study of turbulence, sedimentation, and coignimbrite mass partitioning in dilute pyroclastic density currents. *J. Volcanol. Geotherm. Res.* **225**, 30–44 (2012).
- Brosch, E. et al. Characteristics and controls of the runout behaviour of non-Boussinesq particle-laden gravity currents – A large-scale experimental investigation of dilute pyroclastic density currents. *J. Volcanol. Geotherm. Res.* **432**, 107697 (2022).
- Breard, E. C. P., Lube, G., Cronin, S. J. & Valentine, G. A. Transport and deposition processes of the hydrothermal blast of the 6 August 2012 Te Maari eruption, Mt. Tongariro. *Bull. Volcanol.* **7**, 100 (2015).

20. Dellino, P. et al. Experimental evidence links volcanic particle characteristics to pyroclastic flow hazard. *Earth Planet. Sci. Lett.* **295**, 314–320 (2010).
21. Cole, P. D., et al (Eds.), *The Encyclopedia of Volcanoes*, 943–956, Academic Press (2015).
22. Dellino, P. et al. The impact of pyroclastic density currents duration on humans: the case of the AD 79 eruption of Vesuvius. *Sci. Rep.* **11**, 4959 (2021).
23. Baxter, P. J. et al. Human survival in volcanic eruptions: Thermal injuries in pyroclastic surges, their causes, prognosis and emergency management. *Burns* **43**, 1051–1069 (2017).
24. Pensa, A., Capra, L. & Giordano, G. Ash clouds temperature estimation. Implication on dilute and concentrated PDCs coupling and topography confinement. *Sci. Rep.* **9**, 5657 (2019).
25. Elghobashi, S. On predicting particle-laden turbulent flows. *Appl. Sci. Res.* **52**, 309–329 (1994).
26. Burgisser, A. Physical volcanology of the 2,050 BP caldera-forming eruption of Okmok volcano, Alaska. *Bull. Volcanol.* **67**, 497–525 (2005).
27. Burgisser, A. & Bergantz, G. W. Reconciling pyroclastic flow and surge: the multiphase physics of pyroclastic density currents. *Earth Planet. Sci. Lett.* **202**, 405–418 (2002).
28. Brandt, L. & Coletti, F. Particle-laden turbulence: progress and perspectives. *Ann. Rev. Fluid Mech.* **54**, 159–189 (2021).
29. Breard, E. C. P. et al. Coupling of turbulent and non-turbulent flow regimes within pyroclastic density currents. *Nat. Geosci.* **9**, 767–771 (2016).
30. Breard, E. C. P. & Lube, G. Inside pyroclastic density currents – Uncovering the enigmatic flow structure and transport behaviour in large-scale experiments. *Earth Planet. Sci. Lett.* **458**, 22–36 (2017).
31. Weit, A., Roche, O., Dubois, T. & Manga, M. Experimental measurement of the solid particle concentration in geophysical turbulent gas-particle mixtures. *J. Geophys. Res.* **123**, 2747–2761 (2018).
32. Breard, E. C. P., Dufek, J. & Lube, G. Enhanced mobility in concentrated pyroclastic density currents: An examination of a self-fluidization mechanism. *Geophys. Res. Lett.* **45**: <https://doi.org/10.1002/2017GL075759> (2018).
33. Valentine, G. & Sweeney, M. R. Compressible flow phenomena at inception of lateral density currents fed by collapsing gas-particle mixtures. *J. Volcanol. Geotherm. Res.* **123**, 1286–1302 (2018).
34. Lube, G. et al. Pyroclastic flows generate their own air-lubrication. *Nat. Geosci.* **12**, 381–386 (2019).
35. Brosch, E. & Lube, G. Spatiotemporal sediment transport and deposition in experimental dilute pyroclastic density currents. *J. Volcanol. Geotherm. Res.* **401**, 1–16 (2020).
36. Brosch, E. et al. Destructiveness of pyroclastic surges controlled by turbulent fluctuations. *Nat. Comm.* **12**, 7306 (2021).
37. Clarke, A. B. & Voight, B. Pyroclastic current dynamic pressure from aerodynamics of tree or pole blow-down. *J. Volcanol. Geotherm. Res.* **100**, 395–412 (2000).
38. Baxter, P. J. et al. The impacts of pyroclastic surges on buildings at the eruption of the Soufriere Hills volcano, Montserrat. *Bull. Volcanol.* **67**, 292–313 (2005).
39. Jenkins, S. et al. The Merapi 2010 eruption: An interdisciplinary impact assessment methodology for studying pyroclastic density current dynamics. *J. Volcanol. Geotherm. Res.* **261**, 316–329 (2013).
40. Gardner, J. E., Nazworth, C., Helper, M. A. & Andrews, B. J. Inferring the nature of pyroclastic density currents from tree damage: The 18 May 1980 blast surge of Mount St. Helens, USA. *Geology* **46**, 795–798 (2018).
41. Dellino, P., Mele, D., Sulpizio, R., La Volpe, L. & Braia, G. A method for the calculation of the impact parameters of dilute pyroclastic density currents based on deposit particle characteristics. *J. Geophys. Res.-Solid Earth* **113**, B07206 (2008).
42. Dioguardi, F. & Mele, D. PYFLOW_2.0: a computer program for calculating flow properties and impact parameters of past dilute pyroclastic density currents based on field data. *Bull. Volcanol.* **80**, 28 (2018).
43. Mele, D. et al. Hazard of pyroclastic density currents at the Campi Flegrei Caldera (Southern Italy) as deduced from the combined use of facies architecture, physical modeling and statistics of the impact parameters. *J. Volcanol. Geotherm. Res.* **299**, 35–53 (2015).
44. Lube, G., Breard, E. C. P., Cronin, S. J. & Jones, J. Synthesizing large-scale pyroclastic flows: Experimental design, scaling, and first results from PELE. *J. Geophys. Res.-Solid Earth* **120**, 1487–1502 (2015).
45. Dellino, P. et al. Large-scale experiments on the mechanics of pyroclastic flows: Design, engineering, and first results. *J. Geophys. Res.-Solid Earth* **112**, B04202 (2007).
46. Sulpizio, R., Castioni, D., Rodriguez-Sedano, L. A., Sarocchi, D. & Lucchi, F. The influence of slope-angle ratio on the dynamics of granular flows: insights from laboratory experiments. *Bull. Volcanol.* **78**, 77 (2016).
47. Wilson, C. J. N. The Taupo Eruption, New Zealand. II. The Taupo Ignimbrite. *Philos. Trans. R. Soc. Lond. Ser. A Math. Phys. Sci.* **314**, 229–310 (1985).
48. Bosse, T., Kleiser, L. & Meiburg, E. Small particles in homogeneous turbulence: Settling velocity enhancement by two-way coupling. *Phys. Fluids* **18**, 027102 (2006).
49. Strouhal, V. Ueber eine besondere Art der Tonerregung. *Ann. Phys.* **241**, 216–251 (1878).
50. Turner, J. S. Buoyant plumes and thermals. *Annu. Rev. Fluid Mech.* **1**, 29–44 (1969).
51. Crow, S. C. & Champagne, F. H. Orderly structure in jet turbulence. *J. Fluid Mech.* **48**, 547–591 (1971).
52. Martin, J. E. & Meiburg, E. The accumulation and dispersion of heavy-particles in forced 2-dimensional mixing layers. 1. The fundamental and subharmonic cases. *Phys. Fluids* **6**, 1116–1132 (1994).
53. Raju, N. & Meiburg, E. Dynamics of small, spherical particles in vortical and stagnation point fields. *Phys. Fluids* **9**, 229–314 (1997).
54. Dioguardi, F. & Mele, D. A new shape dependent drag correlation formula for non-spherical rough particles. Experiments and results. *Powder Technol.* **277**, 222–230 (2015).
55. Spence, R. et al. Residential building and occupant vulnerability to pyroclastic density currents in explosive eruptions. *Nat. Hazards Earth Syst. Sci.* **7**, 219–230 (2007).
56. Sovilla, B., McElwaine, J. N. & Köhler, A. The intermittency regions of powder snow avalanches. *J. Geophys. Res.: Earth Surf.* **123**, 2525–2545 (2018).
57. Zhang, F., Frost, D. L., Thibault, P. A. & Murray, S. B. Explosive dispersal of solid particles. *Shock Waves* **10**, 431–443 (2001).
58. Balachandar, S. & Eaton, J. K. Turbulent dispersed multiphase flow. *Annu. Rev. Fluid Mech.* **42**, 111–133 (2010).
59. Capeceelatro, J. & Wagner, J. L. Gas-Particle Dynamics in High-Speed Flows. *Annu. Rev. Fluid Mech.* **3** <https://doi.org/10.1146/annurev-fluid-121021-015818>. (2024)
60. Thielicke, W. & Sonntag, R. Particle Image Velocimetry for MATLAB: Accuracy and Algorithms in PIVlab. *J. Open Res. Softw.* **9**: <https://doi.org/10.5334/jors.334> (2021)
61. Harris, C. R. et al. Array programming with NumPy. *Nature* **585**, 357–362 (2020).
62. Musser, J., Vaidheeswaran, A. & Clarke, M. A. MFX Documentation Volume 3: Verification and Validation Manual; 3rd ed. NETL-PUB-22050; NETL Technical Report Series; U.S. Department of Energy, National Energy Technology Laboratory: Morgantown, WV. (2021).

63. Ducros, F., Nicoud, F. & Poinso, T. Wall-adapting local eddy-viscosity models for simulations in complex geometries. *Numer. Methods Fluid Dyn. VI* **6**, 293–299 (1998).
64. Esposti Ongaro, T., Cerminara, M., Charbonnier, S. J., Lube, G. & Valentine, G. A. A framework for validation and benchmarking of pyroclastic current models. *Bull. Volcanol.* **82**, 51 (2020).
65. Johnson, P. C. & Jackson, R. Frictional-collisional constitutive relations for the granular materials, with application to plane shearing. *J. Fluid. Mech* **176**, 223–233 (1987).
66. Cerminara, M., Brosch, E. & Lube, G. A theoretical framework and the experimental dataset for benchmarking numerical models of dilute pyroclastic density currents. arXiv preprint <https://arxiv.org/abs/2106.14057>. (2021).

Acknowledgements

The authors would like to thank Kevin Kreutz and Anja Moebis for assistance with running the large-scale experiments. This study was partially supported by the Royal Society of New Zealand Marsden Fund (contract no. MAU1902 to GL), the Resilience to Nature's Challenges National Science Challenge Fund New Zealand (GNSRNC047 to GL), the New Zealand Ministry of Business, Innovation and Employment's Endeavour Fund (contract no. GNS-MBIE00216 to GL), the KAVLI Institute of Theoretical Physics Program 'Multiphase Flows in Geophysics and the Environment' (contract no. NSF PHY-1748958 to EM, GL and JD), the National Science Foundation (contract no. NSF EAR-1926025 to JD) and the National Environment Research Council UKRI fund (contract no. NERC-IRF NE/V014242/1 to ECPB).

Author contributions

D.U., J.A., E.B., L.C. and G.L. designed and conducted the experiments. G.L. and D.U. co-wrote the manuscript, which was then revised by all the authors. D.U. led the analysis and interpretation of the experimental data with the help of G.L., E.C.P.B., E.M. and J.R.J., while E.C.P.B. and J.D. conducted and post-processed the numerical simulations. E.B. and J.A. assisted with the P.I.V., flow density and grain-size analyses. S.F.J. and G.L. analysed pockmarks of the Merapi 2010 eruption. G.L. developed the PELE facility together with J.R.J., E.B. and E.C.P.B.

Competing interests

The authors declare no competing interests.

Additional information

Supplementary information The online version contains supplementary material available at <https://doi.org/10.1038/s43247-024-01305-x>.

Correspondence and requests for materials should be addressed to Daniel H. Uhle.

Peer review information *Communications Earth & Environment* thanks Pierfrancesco Dellino, Karim Kelfoun and the other, anonymous, reviewer(s) for their contribution to the peer review of this work. Primary Handling Editors: Domenico Doronzo and Joe Aslin. A peer review file is available

Reprints and permissions information is available at <http://www.nature.com/reprints>

Publisher's note Springer Nature remains neutral with regard to jurisdictional claims in published maps and institutional affiliations.

Open Access This article is licensed under a Creative Commons Attribution 4.0 International License, which permits use, sharing, adaptation, distribution and reproduction in any medium or format, as long as you give appropriate credit to the original author(s) and the source, provide a link to the Creative Commons licence, and indicate if changes were made. The images or other third party material in this article are included in the article's Creative Commons licence, unless indicated otherwise in a credit line to the material. If material is not included in the article's Creative Commons licence and your intended use is not permitted by statutory regulation or exceeds the permitted use, you will need to obtain permission directly from the copyright holder. To view a copy of this licence, visit <http://creativecommons.org/licenses/by/4.0/>.

© The Author(s) 2024